Ternary alloying additions and multilayering as strategies to enhance the galvanic protection ability of Al-Zn coatings electrodeposited from ionic liquid solution

Citation: Cross, Samuel R., and Christopher A. Schuh. "Ternary Alloying Additions and Multilayering as Strategies to Enhance the Galvanic Protection Ability of Al-Zn Coatings Electrodeposited from Ionic Liquid Solution." Electrochimica Acta, vol. 211, Sept. 2016, pp. 860–70.

As Published: https://doi.org/10.1016/j.electacta.2016.06.081

Publisher: Elsevier

Persistent URL: http://hdl.handle.net/1721.1/117527

Version: Author's final manuscript: final author's manuscript post peer review, without publisher's formatting or copy editing

Ternary alloying additions and multilayering as strategies to enhance the galvanic protection ability of Al-Zn coatings electrodeposited from ionic liquid solution

Samuel R. Cross[1], Christopher A. Schuh[1]

1. Department of Materials Science and Engineering, MIT, 77 Massachusetts Avenue, Cambridge, MA USA 02139

Abstract

In recent years, there have been a large number of studies showing that compositionally modulated or multilayer coatings have significantly higher corrosion resistance than monolithic equivalents, in a diverse set of environments. While electrodeposition is an attractive processing method for multilayer coatings, electrodeposition of the aluminum-zinc coatings that would be natural candidates for galvanic corrosion coatings presents several unique challenges. In particular, co-deposition of aluminum and zinc involves a large electrochemical gap between the two elements, low solid solubility, and strong tendency for formation of zinc dendrites. Here we examine the effects of Mn and Zr additions during the electrodeposition of aluminum-zinc from $AlCl_3$/1-ethyl-3-methylimidazolium chloride solution. Aluminum-zinc electrodeposits, with and without addition of Mn or Zr, are prepared and characterized to determine the range of compositions and microstructures that can be produced. The addition of Zr, but not Mn, results in decreased grain size, surface roughness, and compositional homogeneity, as well as the emergence of a nanocrystalline or amorphous phase at low deposition rates. The Al-Zn-Zr electrodeposits also exhibit improved corrosion resistance, as measured by cyclic voltammetry and immersion testing in 50 mM NaCl solution, with additional improvement for multilayered coatings which use the nanocrystalline deposit as a base layer.

1. Introduction

Compositionally modulated coating systems consisting of multiple layers of different metals or alloys have attracted significant interest, due to the potential to obtain improved mechanical or electrochemical properties relative to monolithic coatings of equivalent thickness. In particular, electrodeposited multilayer zinc-based coatings have been shown to be promising candidates for protection of steel substrates, balancing cathodic protection from zinc-rich layers with barrier resistance due to more noble layers [1–6]. The most widely studied system is the Zn-Ni system [2,4–6], in which alternating layers of nickel and zinc have been shown to improve the protection time in salt spray tests by as much as an order of magnitude [2].

In previous computational work by the authors [7], several key elements were identified that contribute to successful performance of multilayer corrosion coatings for sacrificial protection of steel. In particular, coating materials should be effective at inhibiting cathodic reactions, such as oxygen

reduction and hydrogen evolution, and all coating materials should be sacrificial relative to the steel substrate. In addition, for practical use all coating materials should be inexpensive and abundant. Finally, it is desirable to use modest alloying additions that modify the corrosion potential by perhaps 100 mV; by mixing and matching different layers different in potential over this range, substantial galvanic protection benefits are possible.

These criteria are very well satisfied by the aluminum-zinc alloy system, in which zinc provides effective sacrificial protection, while aluminum provides effective barrier protection, but is often found to provide insufficient sacrificial protection to prevent corrosion of steel exposed at defects or cut edges [8,9]. However, to the authors' knowledge, multilayer aluminum-zinc alloys have not yet been investigated for corrosion protection (although interestingly, hot dip aluminum-zinc alloys are by far the most widely employed class of sacrificial coatings for the protection of steel). This may in part be due to significant processing challenges involved in the electrodeposition of aluminum-zinc alloys, which cannot be electrodeposited from aqueous electrolytes due to excessive hydrogen evolution. Although aluminum can be electrodeposited from aluminum chloride-alkali chloride molten salts at high temperatures, such an approach is not promising for synthesis of aluminum-zinc multilayers, as the coating structure would be expected to degrade significantly due to interdiffusion and subsequent phase separation at the plating temperature.

One promising alternative approach to electrodeposition of aluminum-zinc multilayers is through use of room temperature ionic liquids. In particular, ionic liquids consisting of a mixture of $AlCl_3$ and 1-ethyl-3-methylimidazolium chloride (EMIC) have been successfully used to electrodeposit pure aluminum [10–14] as well as a wide range of aluminum alloys, including Al-Zn [15,16], Al-Mn [17–24], Al-Zr [25], and many others [26–37]. In Al-Mn, there is even prior work reporting multilayered coatings, in which the composition and microstructure were controlled between layers through modulation of deposition current density [23,24]. Pan et al. [15,16] reported successful electrodeposition of Al-Zn from $AlCl_3$-EMIC mixtures with 1 wt.% $ZnCl_2$, with compositions ranging from approximately 20 to 100 at.% Zn, depending on the deposition voltage. However, formation of zinc dendrites was observed in the high zinc coatings, leading to a very rough surface and inhomogeneous composition.

Conversely, many secondary alloying elements have been found to improve the properties of aluminum electrodeposits from EMIC/$AlCl_3$ solutions. The most widely studied is Mn, which decreases grain size with increasing concentration, eventually leading to an amorphous structure in deposits with concentrations above approximately 12 at.% Mn, resulting in dramatic improvements in hardness, surface roughness, and corrosion resistance [19,21–23]. Tsuda et al. reported a similar effect for Zr, which was found to produce dual phase deposits with an fcc Al-Zr phase with up to 5 at.% Zr, and an amorphous Al-Zr phase with 17 at.% Zr which showed significant improvement in resistance to pitting corrosion [25]. In one case, the addition of Mn has been shown to have a similar grain refining effect when used as a ternary alloying element in the Al-Mo-Mn system, contributing to the formation of an amorphous metallic phase at above 10 at.% (Mo + Mn), and improving the surface brightness and pitting resistance [30].

In the current study, we have tested the addition of Mn and Zr as ternary alloying additives for Al-Zn electrodeposition from EMIC/$AlCl_3$ solution, and discuss the effects on surface morphology,

microstructure, and corrosion resistance. The binary and ternary alloys are evaluated as candidates for multilayer or functionally graded Al-Zn alloy galvanic coatings.

2. Experimental

Electrodeposition of all aluminum alloys was performed from an anhydrous 2:1 molar mixture of $AlCl_3$ and EMIC (>98%, Iolitec) in a glovebox under an inert nitrogen atmosphere. The ionic liquid was purified for three days through gentle stirring with a strip of pure aluminum (99.99%, Sigma-Aldrich), resulting in a clear light yellow liquid. Anhydrous $ZnCl_2$ was added to a concentration of 0.1 mol l^{-1}. Anhydrous $ZrCl_4$ and $MnCl_2$ were also added to a concentration of 0.02 mol l^{-1} for the Al-Zn-Zr and Al-Zn-Mn baths, respectively. In addition, a separate aqueous bath was prepared for electrodeposition of pure zinc as a comparison material. The composition of the aqueous zinc bath was 1 mol l^{-1} sodium citrate, 0.2 mol l^{-1} zinc sulfate, and 0.001 mol l^{-1} L-cysteine.

The substrates for electrodeposition were 1018 steel (McMaster-Carr) for the immersion corrosion tests, and high purity copper (99.9%, McMaster-Carr) for all other samples. Prior to electrodeposition, each substrate was ground with SiC papers, then polished sequentially with 3, 1, and 0.25 µm diamond polishing compound to obtain a mirror finish, following by ultrasonic degreasing in acetone for 60 seconds. The samples were painted using an enamel spray paint to expose an active area of 1.2 x 2 cm. The samples were then pickled for 30s using 10% H_2SO_4 for the copper and 18% HCl for the steel, dried thoroughly, and placed in a nitrogen-filled glovebox (with oxygen concentration below 2 ppm) for electrodeposition. The steel substrates were activated by 30 seconds of anodic conditioning at 40 Am^{-2} in the electrodeposition bath, just prior to the start of electrodeposition. All electrodeposition was performed galvanostatically in unstirred electrolyte at ambient temperature (23±2 $^{\circ}$C), using a 99.9% Zn strip (Sigma-Aldrich) as an anode. Samples used for characterization of surface morphology and roughness were deposited to a total passed charge of 30 C/cm^2, for a nominal thickness of 8-12 µm. The thickness was measured on a subset of coatings by cross section and in all cases was found to fall within the range of 8-12 µm, suggesting a current efficiency close to 100%. However, there was no systematic study of deposit thickness as a function of deposition parameters, and so the stated thicknesses should be interpreted simply as a range of observed values. Following electrodeposition, the samples were immediately removed from the glovebox, rinsed quickly in deionized water, and dried thoroughly with compressed air.

Adhesion to the substrate was assessed through a tape test performed on a subset of coatings, in which carbon tape was adhered and pulled off of the surface of the deposit. Deposits with no visible loss of material following the tape test were considered to have good adhesion. Characterization of surface morphology and composition was performed using scanning electron microscopy with energy-dispersive spectroscopy (SEM/EDS; JEOL JSM-6610LV). Cross-sections for SEM observation were prepared through focused ion beam milling (FIB; Helios Nanolab 600). The compactness of deposits was assessed through the top-down and, when available, cross section SEM observations, in which no visible voids or pores was considered to indicate a compact deposit. X-ray diffractometry (XRD; X'Pert PANalytical) of electrodeposits was performed using Cu K_α radiation at 45 kV and 40 mA. Measurements

of surface roughness and film thickness were performed using surface contact profilometry (KLA Tencor P-16), with a 2 µm tip diameter and a scan rate of 50 µm s^{-1}. Reported surface roughness values were calculated from the root-mean-square deviation of 51 parallel surface height profiles with 2 µm spacing, covering a 100 x 500 µm region taken from the center of each coating.

Potentiostatic polarization measurements were taken in aerated 50 mM NaCl electrolyte solution, using a standard 3 electrode setup in a Gamry multiport corrosion cell, connected to an AutoLab potentiostat controlled using GPES software. A graphite rod (Gamry) was used as a counter electrode, and potentials were measured using a silver/silver chloride electrode (SSCE; Gamry). Prior to polarization measurements, freshly deposited coatings were immersed in electrolyte solution for 15 minutes while air was gently bubbled through the solution. Anodic polarization curves were then taken at a scan rate of 100 mV/min, starting from at least 200 mV below the open circuit potential, to a maximum potential at least 200 mV above the open circuit potential. The relatively fast scan rate was employed due to the very high dissolution rate at anodic potentials, in order to obtain useful data over a wide potential range without fully dissolving the deposits.

Immersion corrosion tests were performed in naturally aerated 50 mM NaCl electrolyte solution, until the formation of visible red rust on the surface of the coating. Each sample was immersed in a separate container with 200 mL electrolyte, which was refreshed every 48 hours for the duration of the tests. Each sample was gently dipped in DI water for approximately 10 seconds during each electrolyte change to remove excess corrosion products. The corrosion potential of each sample was measured manually every 24 hours using a high-impedance voltmeter (Fluke) and a SSCE reference electrode.

3. Results and discussion

3.1 Al-Zn electrodeposition

Electrodeposition of Al-Zn was performed at constant current densities ranging from 2.4 to 10 mA/cm^2 for a total passed charge density of 30 C/cm^2. All of the tested electrodeposits were compact and showed good adhesion to the substrate. The electrodeposits from 6 to 10 mA/cm^2 had a bright silver surface appearance, while the lower current density deposits had duller surfaces ranging from light gray at 4.8 mA/cm^2 to dark gray at 2.4 mA/cm^2. Particularly at lower current densities, the Al-Zn electrodeposits exhibit a dual-phase microstructure, with zinc dendrites embedded in an aluminum-rich matrix, quite similar to the microstructures reported by Pan et al. [15,16]. As shown in Fig. 1 (a-c), the size and density of the zinc dendrites increases with decreasing current density, ranging from occasional submicron particles in the 8 mA/cm^2 coating to 10 µm zinc dendrites covering much of the surface in the 2.4 mA/cm^2 coating. A close-up of the characteristic matrix-dendrite microstructure, shown in Fig. 1 (d) for the 3.2 mA/cm^2 electrodeposits, illustrates the distinct topographical contrast between the zinc particles and aluminum-rich matrix.

Quantitative surface EDS measurements were taken from several points in the matrix phase and dendrites for each current density. For all of the tested deposits, measured point compositions for the dendrites range from 90-100 at.% Zn, indicating that the dendrites consist almost entirely of Zn. EDS

point measurements of the matrix are spread much more widely, but fall in the range of 10-40 at.% Zn. In addition, a quantitative EDS linescan was taken over a 100 µm interval, to obtain an average composition for each coating. The black circles and error bars in Fig. 2 (a) show the average and standard deviation of the zinc content measured in each EDS linescan. The overall composition is determined primarily by the ratio of the two phases, varying from approximately 25 at.% Zn for the 10 mA/cm^2 electrodeposit to 74 at.% Zn for the 2.4 mA/cm^2 electrodeposit.

By the Faraday equation, the rate of zinc plating r_{Zn} is related to the zinc deposition current density j_{Zn} by:

$$r_{\mathrm{Zn}} = \frac{j_{\mathrm{Zn}}}{z_{Zn}F} \tag{1}$$

where $z_{\mathrm{Zn}} = 2$ is the number of electrons transferred with each deposited atom of zinc, and F is the Faraday constant. Likewise the rate of aluminum plating r_{Al} is given by:

$$r_{\mathrm{Al}} = \frac{j_{\mathrm{Al}}}{z_{\mathrm{Al}}F} \tag{2}$$

where $z_{\mathrm{Al}} = 3$ is the number of electrons transferred with each deposited atom of aluminum. Thus the atomic concentration of zinc in the deposit will be given by:

$$c_{\mathrm{Zn}} = \frac{z_{\mathrm{Zn}} z_{\mathrm{Al}} j_{\mathrm{Zn}}}{z_{\mathrm{Zn}} j_{\mathrm{Al}} + z_{\mathrm{Al}} j_{\mathrm{Zn}}} \tag{3}$$

The dashed line in Fig. 2 (a) shows the Zn composition predicted by Eq. 3 for a constant zinc deposition current of 1.6 mA/cm^2, with Al deposition responsible for the balance. The close agreement with the measured composition of the Al-Zn electrodeposits shows that the rate of zinc deposition is close to this value for all electrodeposition conditions, suggesting that the zinc deposition process is primarily diffusion limited in this system, while Al deposition is primarily activation controlled. However, the low current density electrodeposits show a very large variability in the measured composition over the 100 µm linescans, as illustrated in Fig. 2 (b), which shows a bimodal distribution in composition between points with >90 at.% Zn corresponding to zinc dendrites, and points with 10-40 at.% Zn corresponding to measurements taken at points in the matrix.

3.2 Ternary alloy electrodeposition

Electrodeposition of Al-Zn-Mn and Al-Zn-Zr was performed in identical conditions to the electrodeposition of Al-Zn, with the addition of either 0.02 mol l^{-1} $MnCl_4$ or $ZrCl_4$ to the bath. Visually, the Al-Zn-Mn electrodeposits appeared quite similar to Al-Zn, ranging from a bright silver surface at 10 A/cm^2 to a rough, dark gray surface at 2.4 mA/cm^2. Typical surface morphology for the Al-Zn-Mn electrodeposits is illustrated by SEM micrographs of Al-Zn-Mn deposited at current densities of 8, 4, and 2.4 mA/cm^2 in Fig. 3 (a) - (c). As in the case of Al-Zn, the Al-Zn-Mn electrodeposits exhibit a dual phase microstructure consisting of zinc dendrites embedded in an aluminum-rich matrix, shown in close-up in Fig. 3 (d). However, the microstructure of the Al-Zn-Mn electrodeposits is significantly coarser at lower current densities, and the surface zinc coverage is much greater. The EDS linescan of the Al-Zn-Zr electrodeposit in Fig. 2 (c) shows that while the overall Zn concentration is similar to what was seen in the binary Al-Zn coating, the addition of Zr has substantially decreased the separation of Zn and Al into

distinct phases. The overall Zn composition vs. deposition current density curve for the Al-Zn-Mn electrodeposits, shown as the green squares in Fig. 2 (a) and summarized in Table 1, show a similar trend to that of the Al-Zn deposits, though with a greater range of variation. The Mn content of all films was in the range of 0.5-2 at.%. For the lowest current density deposits, the zinc-rich surface layer was porous and brittle, and could be largely removed through gentle abrasion to reveal an aluminum-rich matrix phase beneath. Thus, the very high Zn content measured through EDS for the lower current density Al-Zn-Mn deposits is more likely a reflection of surface plating of Zn, rather than the true average composition of the deposit. The higher current density deposits, on the other hand, show depletion of Zn relative to the Al-Zn binary deposits. This suggests that ternary alloying with Mn decreases the ability of Zn to incorporate into the aluminum matrix, and instead encourages and exacerbates phase separation within the electrodeposit.

In contrast to Al-Zn and Al-Zn-Mn, the Al-Zn-Zr electrodeposits appeared a dull light gray at all current densities, getting only slightly darker at the lowest current density of 24 Am^{-2}. The average surface composition, shown in Fig. 2 (a), is similar to that of the Al-Zn electrodeposits at the same current density, with the addition of 5-10 at.% Zr. SEM surface micrographs of the Al-Zn-Zr coatings deposited at 8, 4, and 2.4 mA/cm^2 are shown in Fig. 4 (a) - (c). The 8 mA/cm electrodeposit showed a similar character to that of binary Al-Zn deposit at the same current density shown in Fig. 1 (a), with the exception of the appearance of nodules approximately 1-2 μm in diameter. These nodules were not associated with any obvious variation in composition or second phase formation. At lower current densities, the Al-Zn-Zr electrodeposits show rounded crystallites with diameters of up to 4 μm, in clear contrast to the faceted dual-phase microstructures observed in Al-Zn. Such microstructures are generally considered to be highly suggestive of nanocrystalline or amorphous electrodeposits [23]. This conclusion is supported by the XRD spectra for Al-Zn, Al-Zn-Zr, and Al-Zn-Mn electrodeposits, shown in Fig. 5 for a range of current densities. All spectra show clear peaks for Al fcc and Zn hcp phases, as well as the Cu fcc substrate, with the relative intensity of the Al peaks increasing and Zn peaks decreasing with increasing deposition current density. However, the Al-Zn-Zr electrodeposits at low current density also exhibit a low, broad hump in the range 35-45 degrees, as well as decreased intensity for the Al and Zn crystal peaks, suggesting that a significant fraction of the deposit has a nanocrystalline or perhaps even amorphous microstructure.

3.3 Surface roughness

To evaluate electrodeposit surface roughness, 3-D height profiles were taken on 100 x 500 μm regions in the center of a subset of the coatings, using 50 line scans spaced 2 μm apart. Fig. 6 (a) shows a representative 3-D height profile for binary Al-Zn deposited at 4.8 mA/cm^2, while the associated marked line scan is shown in Fig. 6 (b). In both the 3-D and line scans, the dendrites are clearly visible as sharp peaks of up to 6 μm height, while the regions of matrix in between are quite flat and show variations in height of less than 1 μm. Evidently, at least in the case of Al-Zn, the density and size of zinc dendrites is the dominant factor determining the surface roughness. However, the increase in measured surface roughness appears to slow down for deposition rates lower than 4 mA/cm^2, despite the increase Zn content of the coating. This may be due to the very close spacing of the dendrites, which are no longer individually resolvable due to the 2 μm radius of the stylus tip. Therefore, while the

very low current density coatings are very rough, the measured values may underestimate the true roughness value in this regime.

The calculated surface roughness as a function of current density for Al-Zn, Al-Zn-Mn, and Al-Zn-Zr is shown in Fig. 6 (c). The surface roughness results closely mirror the surface morphology observed via SEM. For Al-Zn, the surface roughness increases significantly as the deposition current density drops from 6 to 4 mA/cm^2, which is the same range over which large zinc dendrites become visible in the deposits. The Al-Zn-Mn deposits show a similar, though larger, trend toward increased roughness with decreasing current density, consistent with the increased dendrite formation observed in the low current density Al-Zn-Mn coatings.

The Al-Zn-Zr deposits, however, show virtually no increase in surface roughness down to a deposition current density of 4 mA/cm^2, after which the roughness increases but remains significantly lower than that of Al-Zn. The Al-Zn-Zr deposits do, however, have slightly higher roughness at 6 and 8 mA/cm^2, which is likely due to the nodular surface observed in the micrographs. The full set of measured composition and structural parameters for the binary and ternary electrodeposits is summarized in Table 1.

3.4 Cyclic voltammetry

Because ternary alloying with Zr, but not Mn, was found to significantly improve electrodeposit homogeneity and surface morphology and increase the range of useful deposition rates, we chose to focus on Al-Zn with and without Zr additions as the most viable candidates for use in multilayered corrosion coatings. We limited the corrosion testing to coatings deposited at 4 and 8 mA/cm^2, and for simplicity will refer to the tested coatings according to their composition as measured by EDS. Accordingly, the tested Al-Zn binary alloys are Al59Zn and Al34Zn, and the tested Al-Zn-Zr alloys are Al46Zn8Zr and Al34Zn5Zr, in each case deposited at 4 and 8 mA/cm^2, respectively. The corrosion resistance of the Al-Zn and Al-Zn-Zr electrodeposits was first examined using cyclic voltammetry in aerated 50 mM NaCl solution, as well as pure Al foils (99.99%, Alfa Aesar), a pure Zn electrodeposit from the aqueous Zn solution, and a bare 1018 steel substrate (McMaster).

The cyclic voltammogram of the Al34Zn deposit, shown in Fig. 7 (a), illustrates the typical corrosion behavior observed in these tests. Partial passivity is observed on the first anodic scan, with a rapid increase in current density above a pitting potential of approximately -0.65 V vs SHE. Above the pitting potential, visible gas bubbles emerged from pores in the surface, presumably due to hydrogen evolution from acidified pit interiors. Subsequent scans following the initiation of pitting show reproducible behavior, with moderate anodic current observed for several hundred mV below E_{pit}, increasing rapidly for potentials above E_{pit}. This pattern suggests that the anodic currents below E_{pit} on the second and third scans are due to active dissolution within the interior of pits that were formed during the first scan, while the rapid increase in current density observed above E_{pit} is due to the formation of additional stable pits.

The Al foil was significantly more noble than any of the tested Al-Zn alloys, with a sharp and reproducible pitting transition at $E = -0.38$ V vs SHE. The Zn electrodeposit, on the other hand,

showed weakly passive behavior initially, followed by rapid active dissolution on subsequent scans. In the case of the binary Al-Zn deposits, the dissolution kinetics and measured pitting potential are remarkably similar to that of pure zinc. This is likely due to the presence of zinc particles within the deposit, which are known to act as pitting nucleation sites in Al-Zn alloys [38]. The alloying of 15-30 at.% zinc into the aluminum matrix may also act to destabilize the passive film, resulting in increased susceptibility to pitting. In fact, both of the binary Al-Zn electrodeposits were observed to have dissolved completely after several scans, suggesting that the anodic behavior in the polarization curve is due to the dissolution of the matrix as well as the zinc phase. In addition, the Al59Zn electrodeposit shows markedly greater activity than Al32Zn, with a lower corrosion potential, and faster dissolution kinetics. This is likely due to the higher Zn content, which is generally observed to result in decreased corrosion resistance in Al-Zn alloys [39].

In comparison to the binary Al-Zn deposits, the Al-Zn-Zr deposits show an increase in the pitting potential and a significant decrease in the rate of the dissolution at anodic potentials. Also in contrast to the binary alloy, the Al46Zn8Zr electrodeposit shows improved corrosion resistance relative to Al34Zn5Zr, despite the higher zinc content. The further improvement in corrosion resistance may be due to the transition from a coarse grained to a nanocrystalline or amorphous microstructure, which has been widely reported to increase resistance to localized corrosion [14]. The difference in corrosion susceptibility between the two Al-Zn-Zr deposits suggests that they are promising candidates for use in multilayer coatings for corrosion protection, since the nanocrystalline Al46Zn8Zr layers would be cathodically protected by the Al34Zn5Zr layers, and should therefore act as effective barriers for limiting penetration of corrosion damage, by, for instance, slowing pit propagation, or reducing infiltration of dissolved oxygen to cathodically active sites on the substrate.

3.5 Multilayer Electrodeposits

Fig. 8 shows cross sections of multilayer Al-Zn and Al-Zn-Zr electrodeposits with deposition current density alternating between 8 and 4 mA/cm^2, with 5 C/cm^2 of passed charge for each layer and 30 C/cm^2 for the full deposit, resulting in a total of three layers at each deposition current density. In both cases, the electrodeposits appear compact and well adhered to the substrate. For the Al-Zn deposit in Fig. 8 (a), Zn particles are visible in thin horizontal rows embedded within the Al matrix. Although the density of the Zn particles is higher in the 4 mA/cm^2 layers, it is quite difficult to distinguish distinct layers within the cross section. In comparison, the layered structure of the Al-Zn-Zr deposit in Fig. 8 (b) is much more apparent. Although the layers become rougher as the deposit becomes thicker, they maintain distinctly different microstructures, with the rounded nodular character visible in the 4 mA/cm^2 layers. This suggests that the Al-Zn-Zr electrodeposit may be able to attain superior corrosion protection due to the presence of continuous and distinct barrier layers, while merely varying the phase fractions in the Al-Zn deposit is less likely to produce a continuous barrier following the dissolution of the more susceptible phase.

3.6 Immersion testing

To evaluate the ability of Al-Zn-Zr single and multilayer coatings to protect a steel substrate, immersion corrosion tests were performed on single layer Al-Zn-Zr coatings deposited at 4 and 8

mA/cm^2, denoted according to composition as Al46Zn8Zr and Al32Zn5Zr, respectively, as well as the multilayer deposits with two and four layers formed by alternating between 4 and 8 mA/cm^2. All electrodeposits were plated to a total passed charge of 30 C/cm^2, with the passed charge divided evenly between layers for the multilayer coatings. For simplicity, these multilayer coatings will be denoted by the following shorthand notation:

- M2a, M4a: Al-Zn-Zr multilayer coating with 2 and 4 layers, respectively, produced by alternating the applied current density between 4 and 8 mA/cm^2, with the base layer deposited at 4 mA/cm^2
- M2b, M4b: Al-Zn-Zr multilayer coating with 2 and 4 layers, respectively, produced by alternating the applied current density between 4 and 8 mA/cm^2, with the base layer deposited at 8 mA/cm^2

A pure zinc coating, electrodeposited from the aqueous zinc bath, was included for comparison. The immersion tests were continued until the first visible red rust on the surface of the sample. A description of the tested electrodeposits is included in Table 2, along with the observed protection times for the steel substrate, and the average of the corrosion potentials measured in days 6-10.

During the immersion tests, the corrosion potential of each sample was measured at 24 hour intervals, as shown in Fig. 9. The bare steel electrode was found to have an initial corrosion potential of -0.29 V vs SHE, dropping to a steady state of approximately -0.41 V vs SHE after 72 hours. Thus potentials below the horizontal dotted line in Fig. 9, drawn at -0.51 V, indicate that the coating induces more than 100 mV of cathodic polarization, which is generally considered to signify substantial cathodic protection. The 'x' markings in Fig. 9 indicate the points at which red rust was visible on the surface of the coating, and is considered the point of failure for each coating in this study.

All of the electrodeposited coatings were initially found to provide significant cathodic protection to the steel substrate. The strongest cathodic protection was provided by the pure zinc coating, which had the lowest corrosion potential of all the tested coatings for the first 19 days of the test. During this time the zinc coating became rapidly covered with voluminous white corrosion products, which detached easily from the surface with gentle rinsing. However, the zinc coating also exhibited the shortest lifetime of the tested coatings, with abrupt failure of cathodic protection and red rust formation observed at day 21.

The Al-Zn-Zr single layer electrodeposits, in comparison, exhibited a more modest degree of cathodic protection but substantially increased overall protection time relative to pure zinc. The coarse-grained Al32Zn5Zr deposit had an initial corrosion potential of -0.69 V, which increased to rapidly to -0.60 V after 24 hours, followed by a slow but steady increase to -0.51 V after 38 days. During this period, the coating became covered with a highly adherent layer of black corrosion products. The coating then underwent abrupt failure similar to that observed in the pure zinc coating, with a jump in the corrosion potential to -0.35 V and the immediate formation of visible red rust. The corrosion potential of the nanocrystalline Al46Zn8Zr deposit showed an initially similar pattern, rising quickly from -0.69 to -0.60 V over 5 days, then much more slowly to -0.51 V after 43 days. The surface of the Al46Zn8Zr coating was covered with a highly adherent layer of white corrosion products during this

period. However, whereas the Al32Zn5Zr coating experienced abrupt failure after cessation of cathodic protection, the potential of the Al46Zn8Zr coating drifted up slowly and gradually to that of bare steel, and the formation of red rust was delayed until day 75, just over twice the protection time observed for the Al32Zn5Zr coating.

The observed patterns of corrosion damage to the Al32Zn5Zr and Al46Zn8Zr coatings in Fig. 10 (a-f) show a few characteristic differences. The image of the Al32Zn5Zr coating after 20 days immersion indicates that the coating experienced highly localized damage, with a heterogeneous distribution of corrosion products, and steel substrate visible beneath through-going pits and in areas where the coating had receded from the edges of the sample. Accordingly, the red rust in the image of the Al32Zn5Zr coating after 40 days is largely concentrated in two corners of the sample, while a sizable area in the center remains apparently intact. The corrosion damage to the Al46Zn8Zr coating, by contrast, appeared to occur quite uniformly over the surface, and the image in Fig. 10 (e) shows that even after 40 days the steel substrate was almost completely covered, while the red rust visible in Fig. 10 (f) emerged slowly and uniformly over a large area.

In general, the tested multilayer electrodeposits exhibited improved corrosion protection relative to their monolithic counterparts. The multilayer electrodeposits had cathodic protection times ranging from 51 to 69 days, all of which exceeded the 43 days observed for the highest performing monolithic Al46Zn8Zr coating. In addition, the two deposits M2a and M4a, both of which used the nanocrystalline/amorphous Al46Zn8Zr as a base layer, were able to delay red rust formation for 86 and 90 days respectively, relative to 75 days for the Al46Zn8Zr monolithic coating. However, the two deposits M2b and M4b, which used the coarse-grained Al32Zn5Zr as a base layer, showed red rust after 73 and 59 days, and so both slightly underperformed the monolithic Al46Zn8Zr coating according to this measure. This observed trend is consistent with results in other studies of multilayer corrosion coatings, which generally find that multilayer coatings perform better when more corrosion-resistant materials are used as a base [2,4], and is likely explained by the preferential dissolution of the Al32Zn5Zr base layer, resulting in the undercutting and mechanical failure of the Al46Zn8Zr layers on top. This is supported by a comparison between the corrosion behavior of the M2a and M2b bilayer coatings. While the cathodic protection times for M2a and M2b were very similar, the images of the corroded M2a and M2b coatings in Fig. 10 (g-l) show starkly different distributions of corrosion damage and failure mechanism. The corrosion damage to the M2a coating after 60 days shown in Fig. 10 (h) is almost completely uniform in appearance, while the M2b coating after 60 days shown in Fig. 10 (k) has numerous pits and has receded substantially away from the edge of the sample, exposing steel substrate. Accordingly, in the M2a coating, red rust formation was delayed for 22 days following the loss of cathodic protection, and occurred gradually and uniformly over the surface, as shown in Fig. 10 (i). The M2b coating, in contrast, developed red rust only 8 days after the loss of cathodic protection, and was accompanied by substantial mechanical failure, i.e., visible as cracks in the outer Al46Zn8Zr layer in Fig. 10 (l). The distribution of red rust in Fig. 10 (l) also indicates that the most severe corrosion damage occurred in regions where the outer layer was largely intact, while the exposed steel in the bottom of the image was largely free of red rust. This suggests that the geometry of the M2b bilayer deposit may have exacerbated localized corrosion by causing crevice corrosion in the highly concentrated electrolyte trapped below the intact Al46Zn8Zr barrier layer. The use of the more

resistant Al46Zn8Zr material as a base in the M2a bilayer, conversely, appears to act to distribute corrosion damage more evenly over the surface and delays the exposure of steel substrate, maximizing the useful lifetime of the coating.

4. Conclusion

The following conclusions can be drawn from this investigation of electrodeposition of binary Al-Zn and ternary Al-Zn-Mn and Al-Zn-Mn alloys from $AlCl_3$-EMIC:

- Binary Al-Zn thin films were successfully produced with zinc content ranging from 31 to 75 at.%, and current densities ranging from 2.4 to 10 mA/cm^2. The binary electrodeposits exhibit a dual phase microstructure consisting of a mixture of hcp Zn dendrites and an fcc Al matrix. Dendrite growth is associated with high surface roughness and porosity in the high zinc binary deposits. Zinc dendrite formation would be expected to degrade the properties of single and multilayer aluminum alloy corrosion coatings, by providing initiation points for pit formation, and increasing the chance of through-going pores and defects in the coating.
- The undesirable structure of binary Al-Zn deposits is not improved by ternary alloying with Mn, which instead decreases incorporation of Zn into the Al matrix, resulting in larger zinc dendrites and increased surface roughness for the low current density deposits.
- An improved structure is promoted by ternary alloying with 5-10 at.% Zr, which significantly refines the microstructure and promotes chemical homogeneity in the deposit; XRD peak broadening suggests the formation of nanostructured or even amorphous regions in these deposits. This results in decreased surface roughness for the low current density deposits, with a nodular surface morphology. This structure is viewed as beneficial for corrosion protection. When produced under nominally similar deposition conditions, coarse-grained Al-Zn-Zr electrodeposits have a pitting potential ~40 mV higher than the Al-Zn binary deposits, and when the nanocrystalline/amorphous phase appears in the ternary deposit there is a further increase of ~70 mV in the pitting potential.
- The ternary Al-Zn-Zr electrodeposits have substantially improved ability to protect steel substrates when immersed in 50 mM NaCl solution, delaying the formation of red rust for 75 days, in comparison to 21 days for pure Zn. What is more, such homogeneous alloys can be used to great effect in multilayer stacks that further enhance the protection time. Specifically, multilayer Al-Zn-Zr electrodeposits show additional improvement in protection time up to 90 days for a four layer deposit, when the nanocrystalline/amorphous ternary alloy is used as a base layer.

Based on this work, the Al-Zn-Zr electrodeposition protocol examined here appears to be a viable approach to single-bath Al-Zn alloy coatings, due to the ability to deposit high quality layers, with tunable corrosion properties. This in turn permits the modulation of both composition and microstructure, with demonstrated improvements in corrosion protection as compared with monolithic coatings.

Acknowledgements

This work was sponsored by the BP-MIT Materials and Corrosion Center. The authors would like to thank Richard Woollam, Steven Shademan, and Sai Venkateswaran from BP for their technical guidance. The authors would also like to thank Michael Gibson for his valuable insights into alloy selection. The authors are grateful to Tim McClure, Charles Settens, and Shiahn Chen at the MIT Center for Materials Science, along with many other members of the MIT technical staff, for their assistance with experimental measurements.

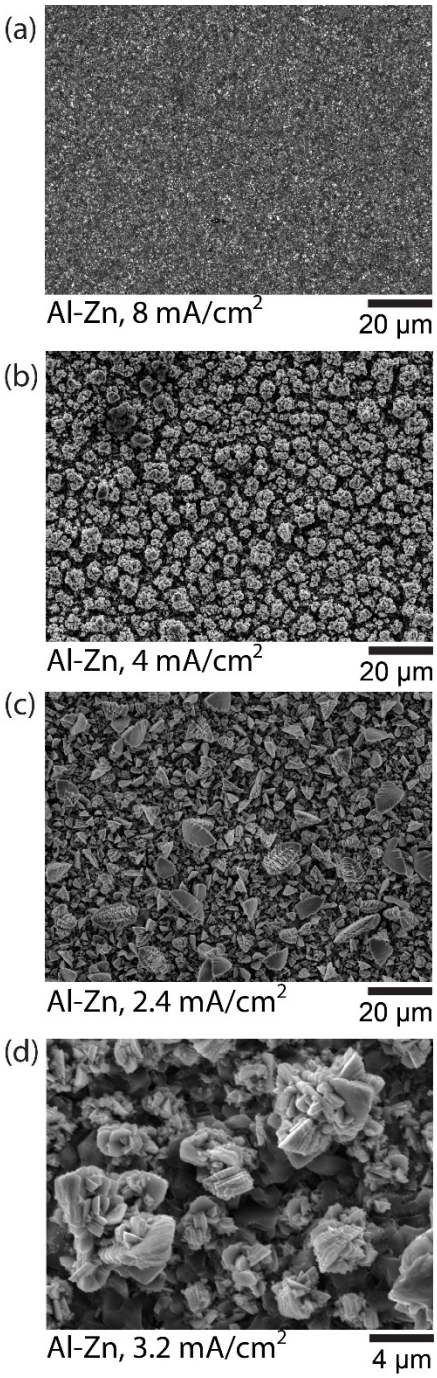

Figure 1.

SEM micrographs of Al-Zn binary electrodeposits for different deposition rates: (a) 8 mA/cm^2, (b) 4 mA/cm^2, and (c) 2.4 mA/cm^2. A close-up of a typical dendrite/matrix microstructure is shown in (d), for a coating deposited at 3.2 mA/cm^2.

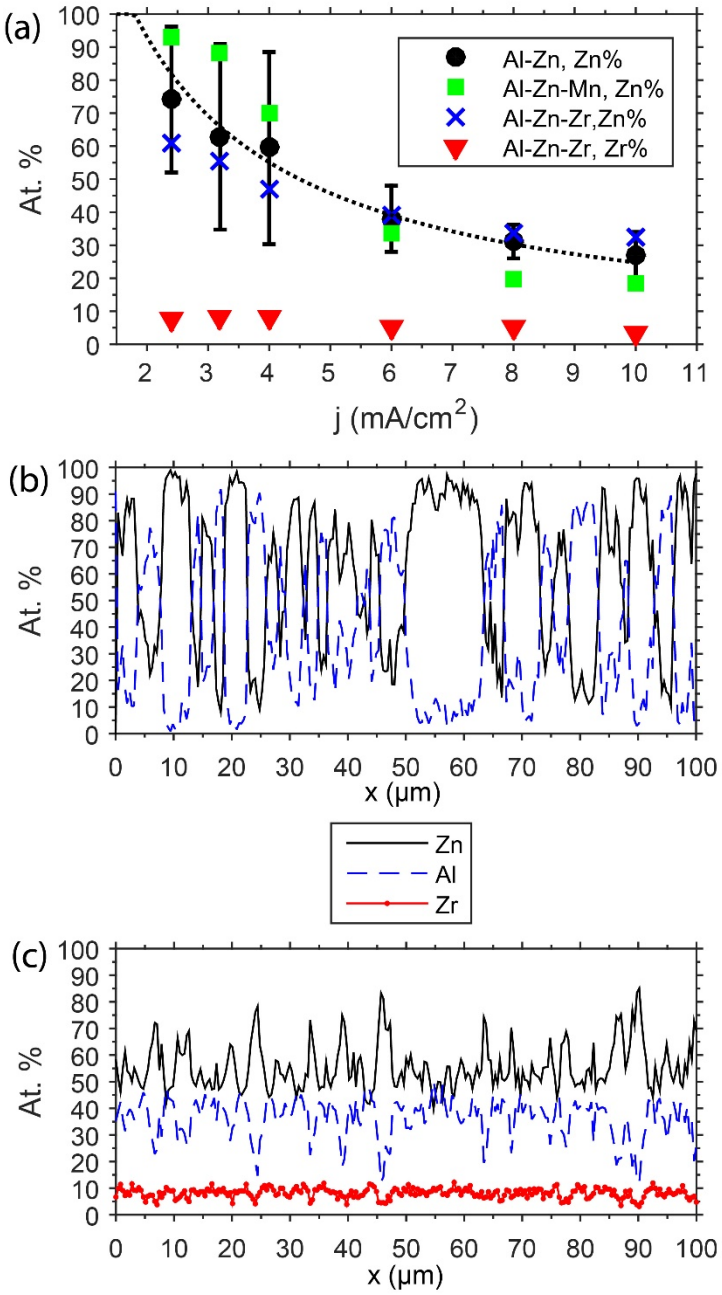

Figure 2.

(a) Surface EDS composition versus deposition current density, for Al-Zn, Al-Zn-Mn, and Al-Zn-Zr electrodeposits. The dotted line indicates the composition calculated according to Eq. 3, for a constant Zn deposition current of 1.6 mA/cm^2. (b) EDS surface composition line scan for an Al-Zn 3.2 mA/cm^2 electrodeposit. (c) EDS surface composition line scan for Al-Zn-Zr 3.2 mA/cm^2 electrodeposit.

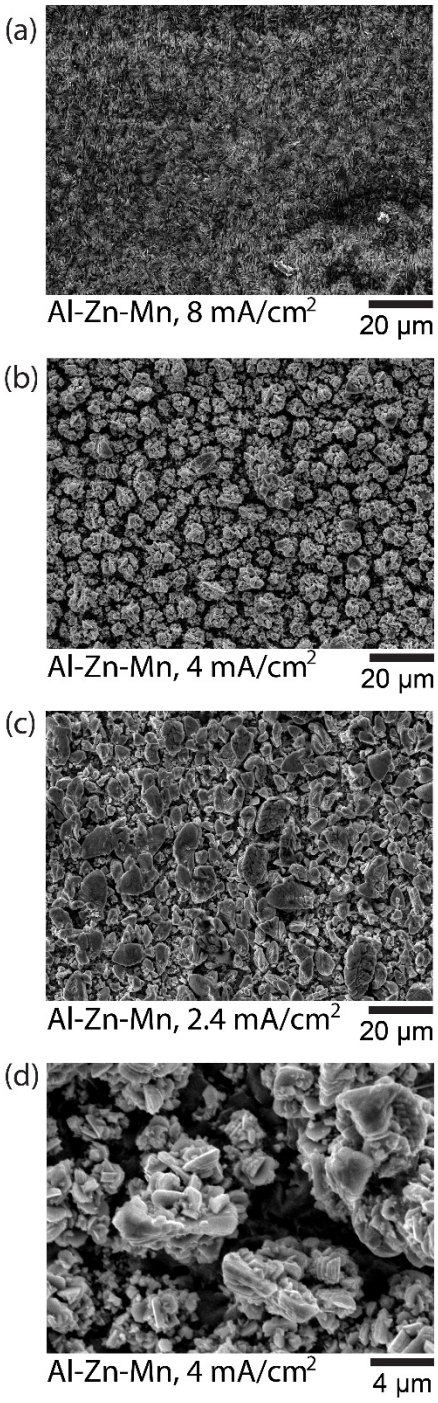

Figure 3.

SEM micrographs of Al-Zn-Mn ternary electrodeposits for different deposition rates: (a) 8 mA/cm^2, (b) 4 mA/cm^2, and (c) 2.4 mA/cm^2. A close-up of a typical dendrite/matrix microstructure is shown in (d), for a coating deposited at 4 mA/cm^2.

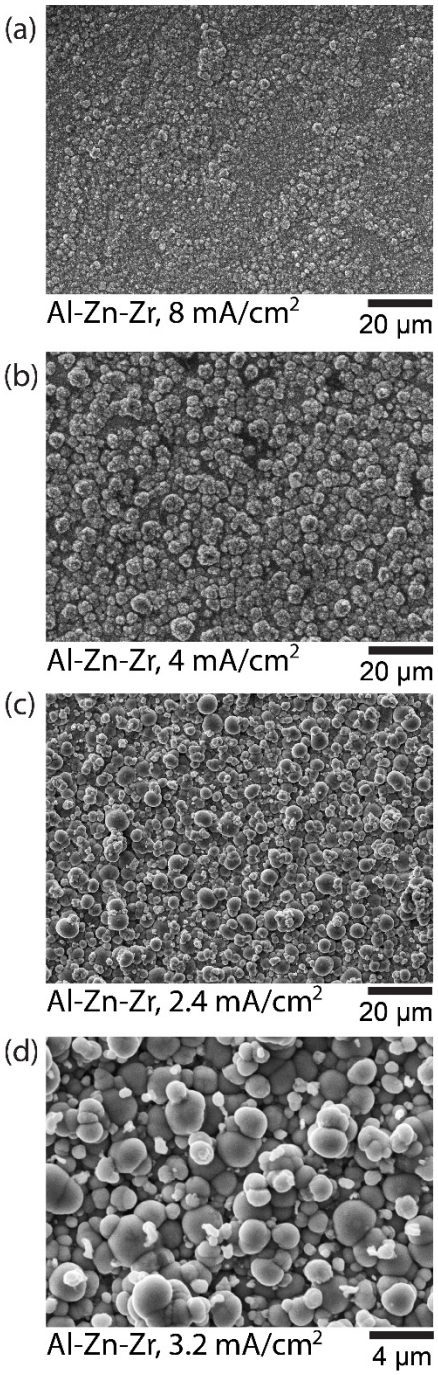

Figure 4.

SEM micrographs of Al-Zn-Zr ternary electrodeposits for different deposition rates: (a) 8 mA/cm^2, (b) 4 mA/cm^2, and (c) 2.4 mA/cm^2. The micrograph (d) for a coating deposited at 3.2 mA/cm^2 shows the nodular surface characteristic of nanocrystalline or amorphous electrodeposits.

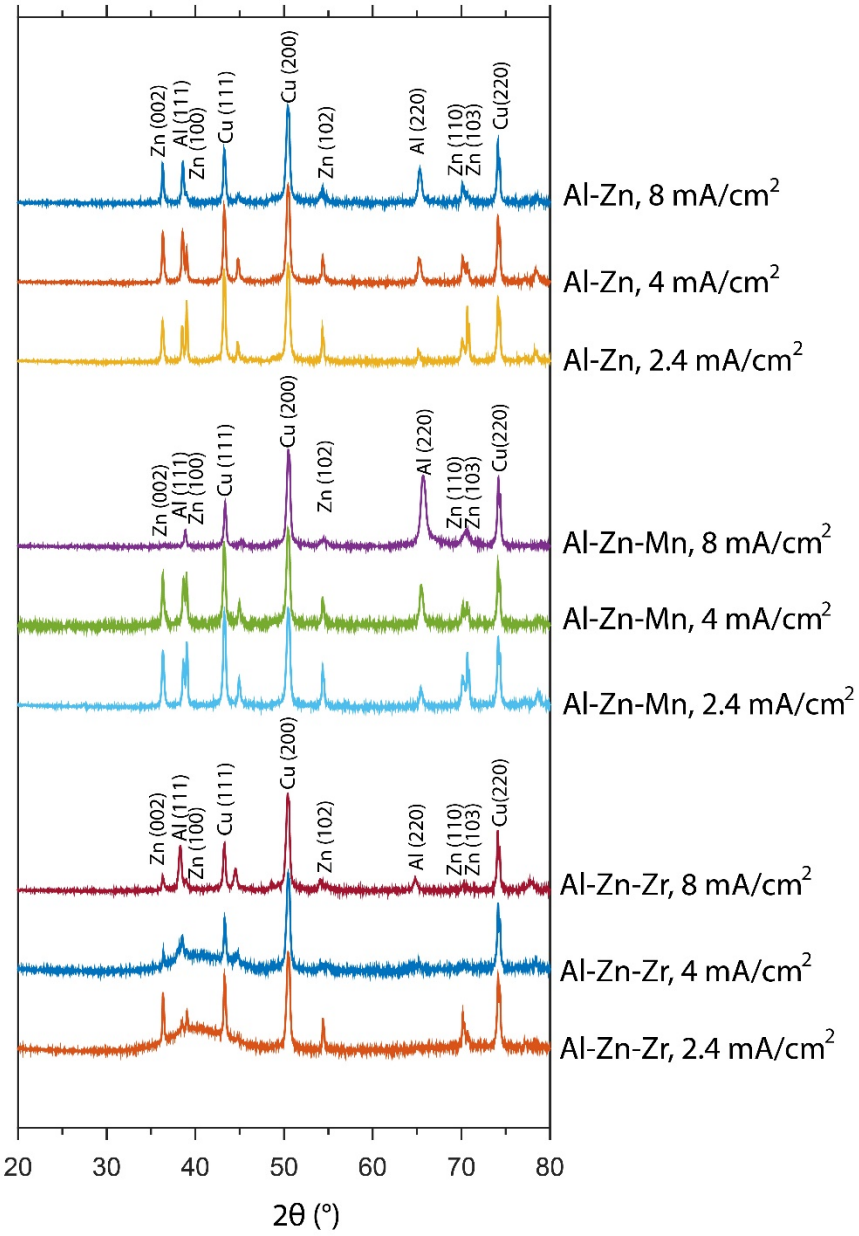

Figure 5.

XRD scans of binary and ternary Al-Zn electrodeposits. The arrows denote the appearance of a broad hump around the nearest-neighbor reflection in the Al-Zn-Zr coatings deposited at 4 and 2.4 mA/cm^2, suggesting a fine nanostructure or an amorphous phase.

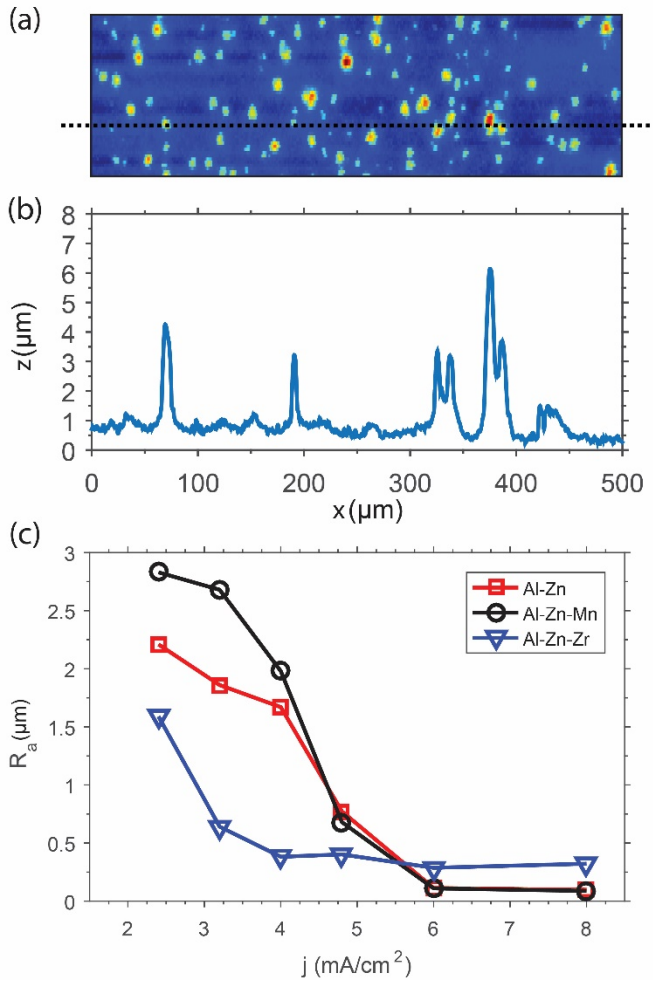

Figure 6.

(a) Surface topography map for a representative Al-Zn coating deposited at 4.8 mA/cm^2. (b) Surface height profile associated with the line marked in (a). (c) Surface roughness measurements for binary and ternary electrodeposits at different deposition current densities.

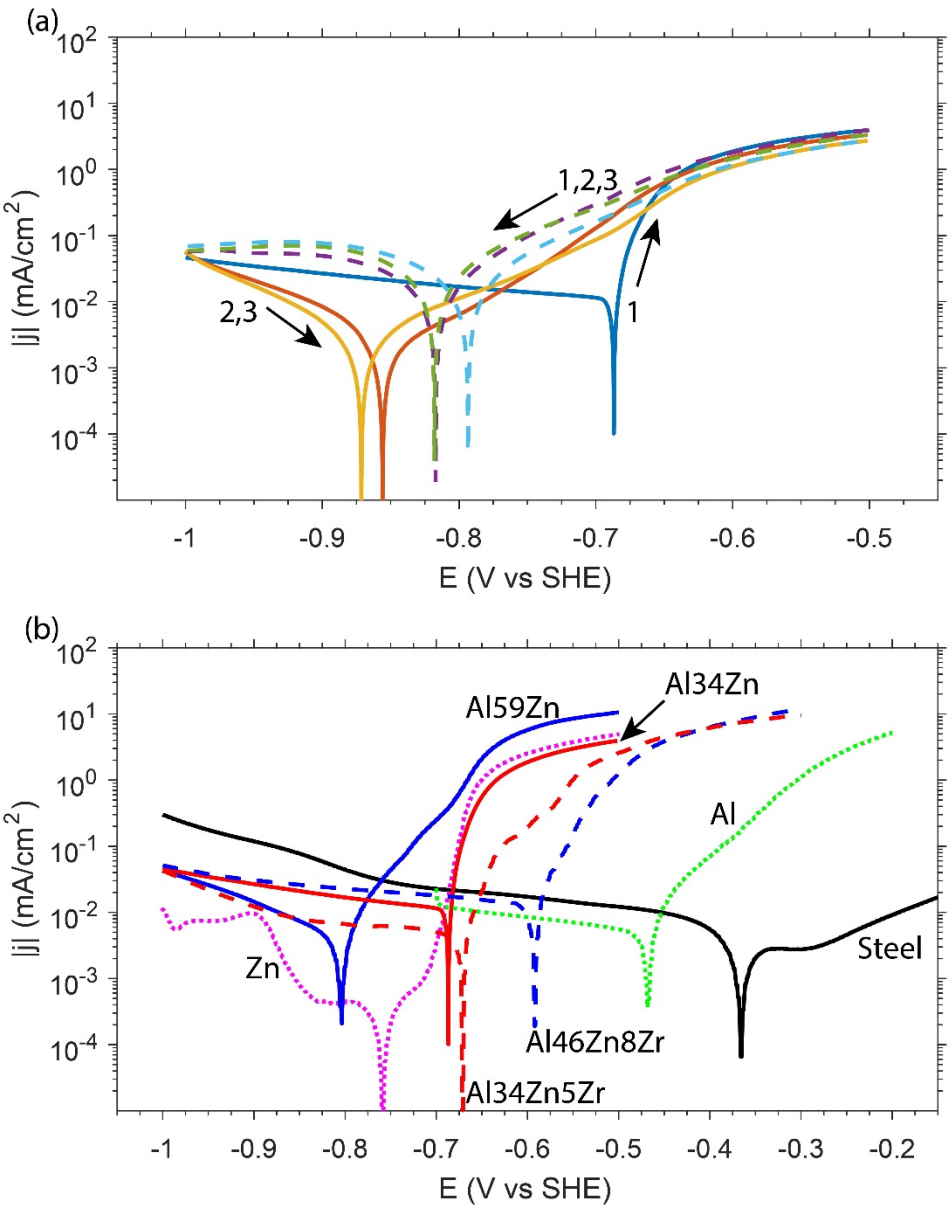

Figure 7.

(a) Cyclic voltammogram for Al34Zn electrodeposit, showing current response to three successive cycles in aerated 50 mM NaCl solution. (b) First anodic scans for binary Al-Zn, ternary Al-Zn-Zr, and reference materials.

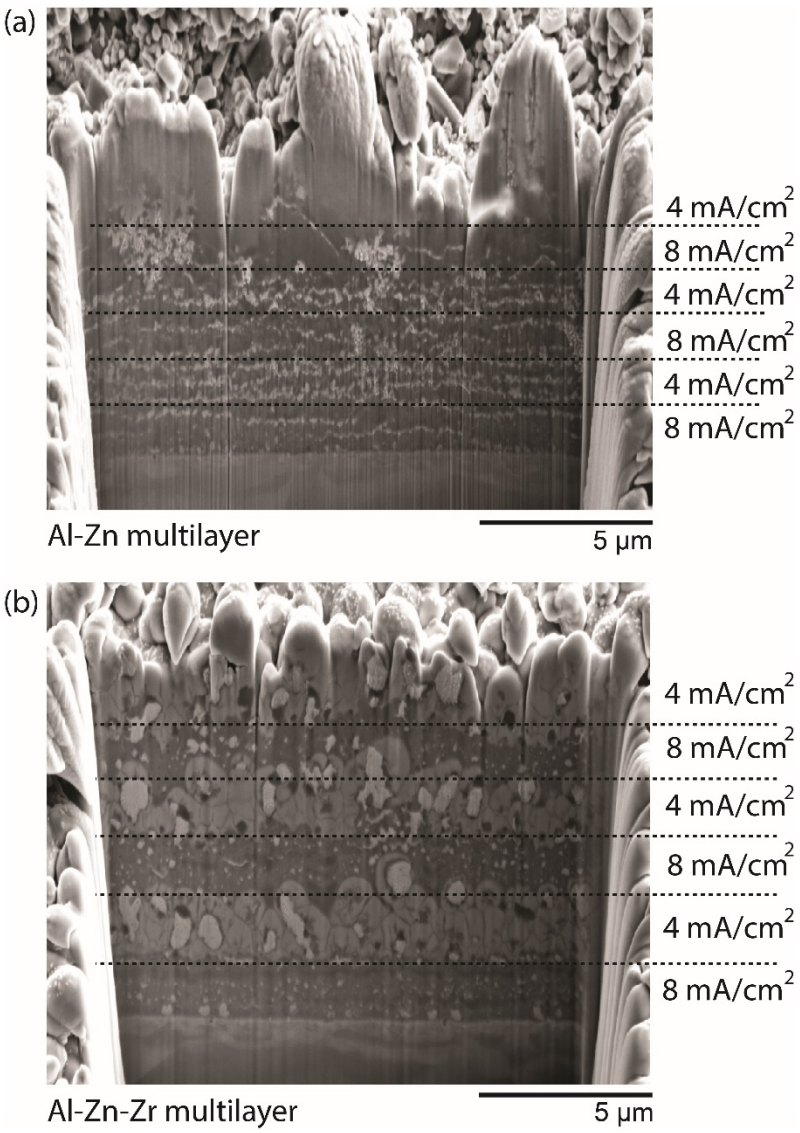

Figure 8.

FIB cross section showing (a) Al-Zn and (b) Al-Zn-Zr multilayer electrodeposits produced through modulation of deposition current density between 4 and 8 mA/cm^2. Dashed lines indicate approximate location of interfaces between layers.

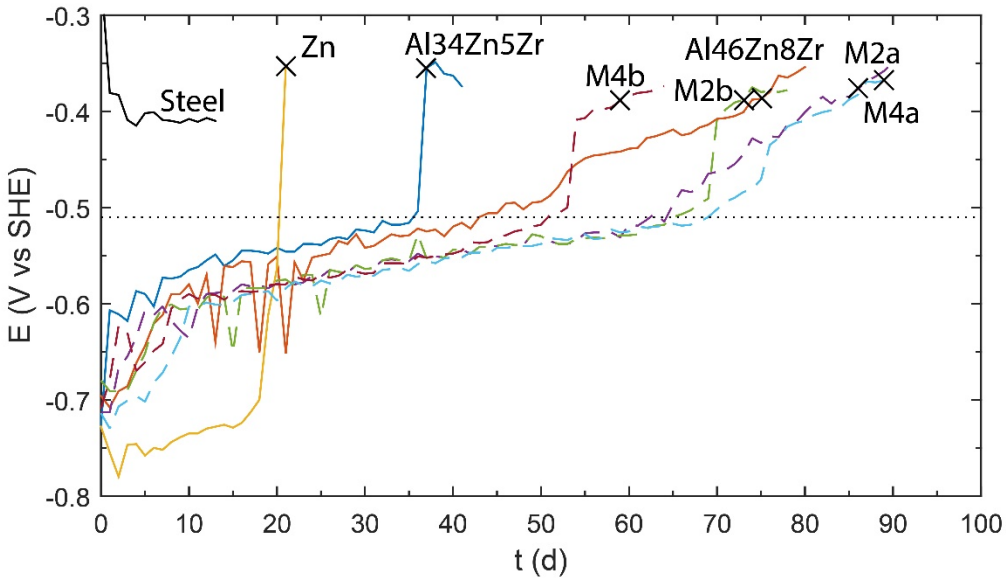

Figure 9

Corrosion potential of Al-Zn-Zr alloy single and multilayer electrodeposits during immersion in 50 mM NaCl solution. The first formation of visible red rust on each coating is marked with an 'x'.

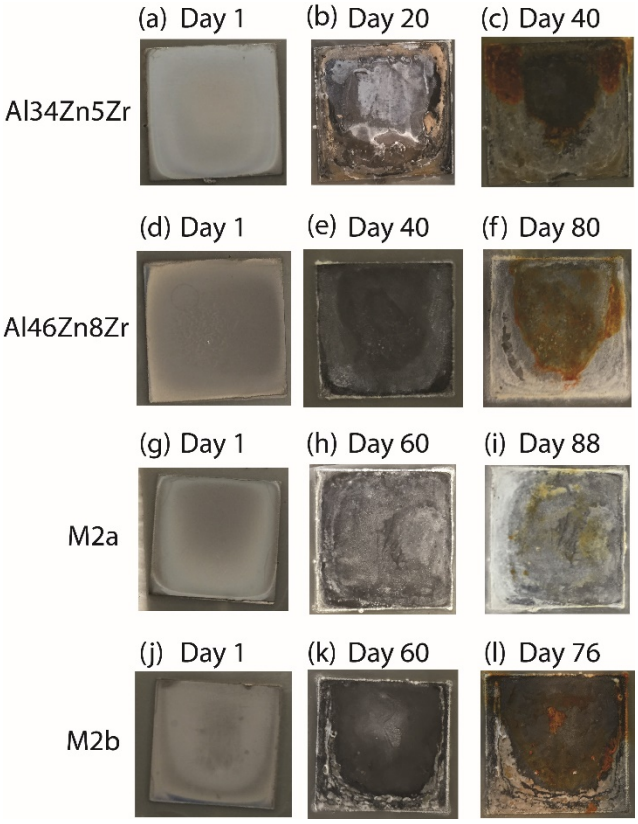

Figure 10:

Images of Al-Zn-Zr electrodeposits following immersion in 50 mM NaCl.

Table 1.

Measured structural and compositional parameters for selected Al-Zn binary and ternary electrodeposits.

Electrodeposit	R_a	Al	Zn	Mn	Zr
Al-Zn 2.4 mA/cm^2	2.21 µm	25.9±22.1 at.%	74.1±22.1 at.%	0	0
Al-Zn 4 mA/cm^2	1.67 µm	40.6±29.1 at.%	59.4±29.1 at.%	0	0
Al-Zn 6 mA/cm^2	0.113 µm	61.8±9.5 at.%	38.2±9.5 at.%	0	0
Al-Zn 8 mA/cm^2	0.097 µm	65.9±4.4 at.%	34.1±4.4 at.%	0	0
Al-Zn-Mn 2.4 mA/cm^2	2.83 µm	6.0±7.7 at.%	93.2±8.4 at.%	0.7±1.2 at.%	0
Al-Zn-Mn, 4 mA/cm^2	1.98 µm	28.3±25.7 at.%	70.1±26.9 at.%	1.5±1.9 at.%	0
Al-Zn-Mn, 6 mA/cm^2	0.108 µm	65.2±2.4 at.%	33.7±2.3 at.%	1.1±0.1 at.%	0
Al-Zn-Mn, 8 mA/cm^2	0.103 µm	79.0±1.1 at.%	19.4±1.0 at.%	1.6±0.1 at.%	0
Al-Zn-Zr 2.4 mA/cm^2	1.59 µm	31.1±12.6 at.%	61.1±14.6 at.%	0	7.8±2.8 at.%
Al-Zn-Zr 4 mA/cm^2	0.382 µm	46.0±5.3 at.%	45.6±4.9 at.%	0	8.4±2.0 at.%
Al-Zn-Zr 6 mA/cm^2	0.287 µm	54.5±3.5 at.%	39.1±3.8 at.%	0	6.4±1.0 at.%
Al-Zn-Zr 8 mA/cm^2	0.322 µm	61.4±4.8 at.%	33.5±4.9 at.%	0	5.0±1.5 at.%

Table 2

Electrodeposits used for 50 mM NaCl immersion testing.

Label	Deposition Protocol	E_{corr}	Cathodic protection	Time to red rust
Zn	4 mA/cm^2, 30 C/cm^2	-0.749 V vs SHE	21 d	21 d
Al34Zn5Zr	8 mA/cm^2, 30 C/cm^2	-0.582 V vs SHE	36 d	37 d
Al46Zn8Zr	4 mA/cm^2, 30 C/cm^2	-0.611 V vs SHE	43 d	75 d
M2a	4 mA/cm^2, 15 C/cm^2 8 mA/cm^2, 15 C/cm^2	-0.614 V vs SHE	64 d	86 d
M2b	8 mA/cm^2, 15 C/cm^2 4 mA/cm^2, 15 C/cm^2	-0.617 V vs SHE	65 d	73 d
M4a	4 mA/cm^2, 7.5 C/cm^2 8 mA/cm^2, 7.5 C/cm^2 4 mA/cm^2, 7.5 C/cm^2 8 mA/cm^2, 7.5 C/cm^2	-0.669 V vs SHE	69 d	89 d
M4b	8 mA/cm^2, 7.5 C/cm^2 4 mA/cm^2, 7.5 C/cm^2 8 mA/cm^2, 7.5 C/cm^2 4 mA/cm^2, 7.5 C/cm^2	-0.631 V vs SHE	51 d	59 d

[1] I. Kirilova, I. Ivanov, Corrosion behaviour of Zn-Co compositionally modulated multilayers electrodeposited from single and dual baths, J. Appl. Electrochem. 29 (1999) 1133–1137. doi:10.1023/A:1003675216529.
[2] J. Fei, G.D. Wilcox, Electrodeposition of zinc–nickel compositionally modulated multilayer coatings and their corrosion behaviours, Surf. Coat. Technol. 200 (2006) 3533–3539. doi:10.1016/j.surfcoat.2004.08.183.
[3] N. Boshkov, K. Petrov, G. Raichevski, Corrosion behavior and protective ability of multilayer Galvanic coatings of Zn and Zn-Mn alloys in sulfate containing medium, Surf. Coat. Technol. 200 (2006) 5995–6001. doi:10.1016/j.surfcoat.2005.10.002.
[4] M. Rahsepar, M.E. Bahrololoom, Corrosion study of Ni/Zn compositionally modulated multilayer coatings using electrochemical impedance spectroscopy, Corros. Sci. 51 (2009) 2537–2543. doi:10.1016/j.corsci.2009.06.030.
[5] M. Rahsepar, M.E. Bahrololoom, Study of surface roughness and corrosion performance of Ni/Zn–Fe and Zn–Fe/Ni compositionally modulated multilayer coatings, Surf. Coat. Technol. 204 (2009) 580–585. doi:10.1016/j.surfcoat.2009.08.036.
[6] A. Maciej, G. Nawrat, W. Simka, J. Piotrowski, Formation of compositionally modulated Zn–Ni alloy coatings on steel, Mater. Chem. Phys. 132 (2012) 1095–1102. doi:10.1016/j.matchemphys.2011.12.074.
[7] S.R. Cross, R. Woollam, S. Shademan, C.A. Schuh, Computational design and optimization of multilayered and functionally graded corrosion coatings, Corros. Sci. 77 (2013) 297–307. doi:10.1016/j.corsci.2013.08.018.
[8] M. Natesan, G. Venkatachari, N. Palaniswamy, Kinetics of atmospheric corrosion of mild steel, zinc, galvanized iron and aluminium at 10 exposure stations in India, Corros. Sci. 48 (2006) 3584–3608. doi:10.1016/j.corsci.2006.02.006.
[9] T.A. Lowe, G.G. Wallace, A.K. Neufeld, Insights into the cut edge corrosion of 55% Al-Zn metal coating on steel from simultaneous electrochemical polarization and localised pH sensing experiments, Corros. Sci. 55 (2012) 180–186. doi:10.1016/j.corsci.2011.10.015.
[10] J.J. Lee, I.T. Bae, D.A. Scherson, B. Miller, K.A. Wheeler, Underpotential deposition of aluminum and alloy formation on polycrystalline gold electrodes from AlCl3/EMIC room-temperature molten salts, J. Electrochem. Soc. 147 (2000) 562–566. doi:10.1149/1.1393233.
[11] J.-K. Chang, S.-Y. Chen, W.-T. Tsai, M.-J. Deng, I.-W. Sun, Electrodeposition of aluminum on magnesium alloy in aluminum chloride (AlCl3)–1-ethyl-3-methylimidazolium chloride (EMIC) ionic liquid and its corrosion behavior, Electrochem. Commun. 9 (2007) 1602–1606. doi:10.1016/j.elecom.2007.03.009.
[12] D. Pradhan, D. Mantha, R.G. Reddy, The effect of electrode surface modification and cathode overpotential on deposit characteristics in aluminum electrorefining using EMIC-AlCl3 ionic liquid electrolyte, Electrochimica Acta. 54 (2009) 6661–6667. doi:10.1016/j.electacta.2009.06.059.
[13] J. Tang, K. Azumi, Optimization of pulsed electrodeposition of aluminum from AlCl3-1-ethyl-3-methylimidazolium chloride ionic liquid, Electrochimica Acta. 56 (2011) 1130–1137. doi:10.1016/j.electacta.2010.10.056.
[14] A. Bakkar, V. Neubert, Electrodeposition and corrosion characterisation of micro- and nano-crystalline aluminium from AlCl3/1-ethyl-3-methylimidazolium chloride ionic liquid, Electrochimica Acta. 103 (2013) 211–218. doi:10.1016/j.electacta.2013.03.198.
[15] S.-J. Pan, W.-T. Tsai, J.-K. Chang, I.-W. Sun, Co-deposition of Al-Zn on AZ91D magnesium alloy in AlCl3-1-ethyl-3-methylimidazolium chloride ionic liquid, Electrochimica Acta. 55 (2010) 2158–2162. doi:10.1016/j.electacta.2009.11.050.

[16] S.-J. Pan, W.-T. Tsai, I.-W. Sun, Electrodeposition of Al–Zn on Magnesium Alloy from ZnCl2-Containing Ionic Liquids, Electrochem. Solid-State Lett. 13 (2010) D69–D71. doi:10.1149/1.3447842.
[17] T. Moffat, G. Stafford, D. Hall, Pitting Corrosion of Electrodeposited Aluminum-Managanese Alloys, J. Electrochem. Soc. 140 (1993) 2779–2786. doi:10.1149/1.2220910.
[18] H.C. De Long, J.A. Mitchell, P.C. Trulove, Investigations of the electrodeposition of aluminum-manganese alloys from room temperature chloroaluminate molten salts, High Temp. Mater. Process. 2 (1998) 507–519.
[19] P.C. Trulove, J.A. Mitchell, P.L. Hagans, R.T. Carlin, G.R. Stafford, H.C. De Long, Electrodeposition and pitting corrosion of aluminum-manganese alloys from room temperature chloroaluminate molten salts, Electrochemical Society Inc, Pennington, 2000.
[20] J. Zhang, W. Zhang, C. Yan, K. Du, F. Wang, Corrosion behaviors of Zn/Al–Mn alloy composite coatings deposited on magnesium alloy AZ31B (Mg–Al–Zn), Electrochimica Acta. 55 (2009) 560–571. doi:10.1016/j.electacta.2009.09.026.
[21] S. Ruan, C.A. Schuh, Electrodeposited Al-Mn alloys with microcrystalline, nanocrystalline, amorphous and nano-quasicrystalline structures, Acta Mater. 57 (2009) 3810–3822. doi:10.1016/j.actamat.2009.04.030.
[22] J. Chen, B. Xu, G. Ling, Amorphous Al-Mn coating on NdFeB magnets: Electrodeposition from AlCl3-EMIC-MnCl2 ionic liquid and its corrosion behavior, Mater. Chem. Phys. 134 (2012) 1067–1071. doi:10.1016/j.matchemphys.2012.03.114.
[23] W. Cai, C.A. Schuh, Tuning nanoscale grain size distribution in multilayered Al-Mn alloys, Scr. Mater. 66 (2012) 194–197. doi:10.1016/j.scriptamat.2011.10.040.
[24] W. Cai, C.A. Schuh, Microstructure and mechanical properties of electrodeposited Al1-xMnx/Al1-yMny nanostructured multilayers, J. Mater. Res. 29 (2014) 2229–2239. doi:10.1557/jmr.2014.238.
[25] T. Tsuda, C.L. Hussey, G.R. Stafford, O. Kongstein, Electrodeposition of Al-Zr alloys from lewis acidic aluminum chloride-1-ethyl-3-methylimidazolium chloride melt, J. Electrochem. Soc. 151 (2004) C447–C454. doi:10.1149/1.1753231.
[26] R.T. Carlin, P.C. Trulove, H.C. DeLong, Electrodeposition of cobalt-aluminum alloys from room temperature chloroaluminate molten salt, J. Electrochem. Soc. 143 (1996) 2747–2758. doi:10.1149/1.1837102.
[27] D.E. Clinton, P.C. Trulove, P.L. Hagans, H.C. De Long, Electrodeposition and nucleation studies of chromium from an acidic ambient temperature chloroaluminate molten salt, Electrochemical Society Inc, Pennington, 1998.
[28] M. Morimitsu, N. Tanaka, M. Matsunaga, Induced codeposition of Al-Mg alloys in Lewis acidic AlCl3-EMIC room temperature molten salts, Chem. Lett. (2000) 1028–1029. doi:10.1246/cl.2000.1028.
[29] T. Tsuda, C.L. Hussey, G.R. Stafford, J.E. Bonevich, Electrochemistry of titanium and the electrodeposition of Al-Ti alloys in the Lewis acidic aluminum chloride-1-ethyl-3-methylimidazolium chloride melt, J. Electrochem. Soc. 150 (2003) C234–C243. doi:10.1149/1.1554915.
[30] T. Tsuda, C.L. Hussey, G.R. Stafford, Electrodeposition of Al-Mo-Mn ternary alloys from the Lewis acidic AlCl3-EtMeImCl molten salt, J. Electrochem. Soc. 152 (2005) C620–C625. doi:10.1149/1.1995696.
[31] T. Tsuda, S. Arimoto, S. Kuwabata, C.L. Hussey, Electrodeposition of Al-Mo-Ti ternary alloys in the Lewis acidic aluminum chloride-1-ethyl-3-methylimidazolium chloride room-temperature ionic liquid, J. Electrochem. Soc. 155 (2008) D256–D262. doi:10.1149/1.2833305.

[32] T. Gandhi, K.S. Raja, M. Misra, Room temperature electrodeposition of aluminum antimonide compound semiconductor, Electrochimica Acta. 53 (2008) 7331–7337. doi:10.1016/j.electacta.2008.04.014.
[33] B. Li, C. Fan, Y. Chen, J. Lou, L. Yan, Pulse current electrodeposition of Al from an AlCl3-EMIC ionic liquid, Electrochimica Acta. 56 (2011) 5478–5482. doi:10.1016/j.electacta.2011.03.047.
[34] A. Lahiri, R. Das, Spectroscopic studies of the ionic liquid during the electrodeposition of Al-Ti alloy in 1-ethyl-3-methylimidazolium chloride melt, Mater. Chem. Phys. 132 (2012) 34–38. doi:10.1016/j.matchemphys.2011.10.048.
[35] T. Tsuda, Y. Ikeda, T. Arimura, A. Imanishi, S. Kuwabata, C.L. Hussey, G.R. Stafford, Al-W Alloy Deposition from Lewis Acidic Room-Temperature Chloroaluminate Ionic Liquid, Molten Salts Ion. Liq. 18. 50 (2012) 239–250. doi:10.1149/05011.0239ecst.
[36] T. Tsuda, S. Kuwabata, G.R. Stafford, C.L. Hussey, Electrodeposition of aluminum-hafnium alloy from the Lewis acidic aluminum chloride-1-ethyl-3-methylimidazolium chloride molten salt, J. Solid State Electrochem. 17 (2013) 409–417. doi:10.1007/s10008-012-1933-y.
[37] T. Tsuda, Y. Ikeda, T. Arimura, M. Hirogaki, A. Imanishi, S. Kuwabata, G.R. Stafford, C.L. Hussey, Electrodeposition of Al-W Alloys in the Lewis Acidic Aluminum Chloride-1-Ethyl-3-Methylimidazolium Chloride Ionic Liquid, J. Electrochem. Soc. 161 (2014) D405–D412. doi:10.1149/2.016409jes.
[38] N. Peng, Y. He, H. Song, X. Yang, X. Cai, Effects of electrodeposited Zn nuclei on tunnel etching behavior of aluminum foil, Corros. Sci. 91 (2015) 213–219. doi:10.1016/j.corsci.2014.11.023.
[39] W. Chen, Q. Liu, Q. Liu, L. Zhu, L. Wang, A combinatorial study of the corrosion and mechanical properties of Zn–Al material library fabricated by ion beam sputtering, J. Alloys Compd. 459 (2008) 261–266. doi:10.1016/j.jallcom.2007.05.046.